The structural response of the thermoplastic composite joint subjected to out-of-plane loading

Chao Chen , Changze Sun , Xu Han , Dean Hu , Jin Zhou , Zhongwei Guan

PII: S0734-743X(20)30761-2
DOI: https://doi.org/10.1016/j.ijimpeng.2020.103691
Reference: IE 103691

To appear in: *International Journal of Impact Engineering*

Received date: 14 January 2020
Revised date: 29 June 2020
Accepted date: 7 August 2020

Please cite this article as: Chao Chen , Changze Sun , Xu Han , Dean Hu , Jin Zhou , Zhongwei Guan , The structural response of the thermoplastic composite joint subjected to out-of-plane loading, *International Journal of Impact Engineering* (2020), doi: https://doi.org/10.1016/j.ijimpeng.2020.103691

Highlights

- Impact responses of the thermoplastic composite single-lap double rivet joints with and without adhesive
- Strain-rate effects and damage evolution on the joint response are considered
- Studies on the effects of the boundary condition, ply angle and impact energy in the impact resistance

The structural response of the thermoplastic composite joint subjected to out-of-plane loading

Chao Chen[a,b], Changze Sun [b], Xu Han[a,c], Dean Hu[a*], Jin Zhou[b,d], Zhongwei Guan[b,e]

[a]*State Key Laboratory of Advanced Design and Manufacturing for Vehicle Body, Hunan University, Changsha 410082, P. R. China*

[b]*School of Engineering, University of Liverpool, Liverpool L69 3GH, United Kingdom*

[c]*School of Mechanical Engineering, Hebei University of Technology, Tianjin 300401, P. R.China*

[d]*School of Mechanical Engineering, Xi'an Jiaotong University, Xi'an, 710049, P. R. China*

[e]*School of Mechanical Engineering, Chengdu University, Chengdu 610106, China*

Corresponding author: *Dean Hu* (hudean@hnu.edu.cn)

Abstract: This paper presents a study on thermoplastic single-lap double rivet joints (SLDJ) with and without adhesive subjected to out-of-plane projectile impact and quasi-static concentrated loading. The three-dimensional finite element (FE) models considering strain-rate effects and damage evolution were developed and implemented in the commercial code Abaqus/Explicit through a user-defined subroutine VUMAT. The FE models were validated against the experimental results, in terms of the peak load, the maximum displacement and the dissipated energy. It was found that there were three stages in the load-displacement trace up to the failure, i.e. rivet slip, hole failure and laminate break for the rivet joint, and debonding, rivet slip and laminate break for the rivet joint with adhesive. The rivet joint with adhesive has a higher stiffness before debonding occurs; however, its out-of-plane load carrying capacity is slightly lower than the rivet only counterpart. The validated models were used to study the failure mechanisms of SLDJ through the progressive failure simulation, and further to investigate the effects of boundary conditions, ply angle and impact energy on the impact response of the composite joints. The laminates with 45° ply could be used to enhance the impact resistance of composite joint structures with the reduced damaged area.

Keywords

Thermoplastic composite joint; Out-of-plane impact; Finite element; User-defined subroutine

1. Introduction

Continuous fibre reinforced thermoset composite materials have been widely used in the automotive industry with increasing demands on lightweight design and components [1-3]. However, in accordance with the law issued by the European Union in 2015, which is also followed rapidly by other countries, 95% of materials for a new car must be recyclable [1, 3]. Compared with traditional thermoset composites, continuous fibre-reinforced thermoplastics (CFRTPs) have more design merits, such as abilities to be re-melted, remoulded and re-used. Thus, CFRTPs are becoming more attractive for the automotive industry than the thermoset equivalents [1].

The joining method is one of the primary technical challenges on composite material applications in the automotive industry [4]. The bolted joint is a common form of joints, but with stress concentration around the hole. Adhesively bonded joints generally result in a catastrophic "no-warning" failure. If a high degree of end restraint is required, the combined bolted/bonded joint will be efficient. Out-of-plane impact strength is a matter of interest in vehicle engineering. Vehicles must provide an adequate safety level for their occupants when it encounters side-impact, rolling and pillar impact collisions, as shown in Fig. 1. Understanding the structural behaviour of composite joint under out-of-plane loading conditions is therefore crucial for designing reliable and safe composite structures.

(a) A-pillar-cross reinforcing components (b) B-pillar core reinforcing components

Fig. 1. Composite joint structures of BMW 7 series may encounter transverse loading [5].

A number of researchers analysed composite joints experimentally and numerically when they were subjected to in-plane tension loading [6-12]. McCarthy et al. [6] carried out the 3D finite element analysis

of single-lap bolted joints under quasi-static tensile loading condition. Ger et al. [7] tested composite material joints with different configurations subjected to quasi-static tensile loading and dynamic loading with tensile velocities between 3 and 5 m/s. It was reported that the joint stiffness increased with the loading rate, but the energy absorption and the ultimate load had no general trend. These conclusions were commented by Li et al. [8] as the inertia effects was not considered. Li et al. [8] also investigated the dynamic characteristics of the composite rivet joint subjected to in-plane tensile loading rate up to 8 m/s. They concluded that the strength values depended on the joint configuration and loading rate. Pearce et al. [9] observed a change of failure modes with an increasing tensile loading rate over 1 m/s. Egan et al. [10] and Heimbs et al. [11] tested composite bolted joints at a higher in-plane tensile loading rate up to 10 m/s, with a significantly higher energy absorption being observed. Also, Perogamvros et al. [12] performed a range of experiments on composite joints with lockbolt fasteners subjected to in-plane quasi-static tension and in-plane low-velocity impact (up to 2.8 m/s). They observed the elevated energy absorption values in dynamic conditions, with different failure modes and failure loads.

Croxford et al.[13], Song et al. [14] and Chen et al. [15] undertook research on hole eccentricity and tolerance of composite bolted joints under a quasi-static in-plane tension condition. Meanwhile, limited studies were focused on the transverse impact response of thermoset composite joints in the adhesively-bonded overlap region, such as woven glass/epoxy [16, 17], woven glass/phenolic [18], unidirectional carbon/epoxy [19] and woven carbon/epoxy [20, 21]. Kim et al. [16] investigated the adhesively bonded composite joints subjected to transverse impact using a drop-weight tower with a velocity range from 2.71 to 6.32 m/s. Sayman et al. [17] also experimentally evaluated the shear strength of adhesively bonded joints under different temperatures (-20 °C, 23 °C, 50 °C and 80 °C) and

transverse impact energies (5, 10, 15 and 20 J). Choudhry et al. [18] studied transverse impact response of the adhesively bonded composite joints with different overlap widths in an energy range of 1.6 J to 8 J. Park and Kim [19] focused on the damage resistance and failure threshold energy of the adhesively bonded joints subjected to high velocity (116.7 m/s) transverse ice impact. Wu et al. [20] investigated the crashworthiness of adhesively bonded composite joints in vehicle structures, with different overlap length and width being studied. Liu et al. [21] further studied the residual properties of adhesively bonded composite and aluminium joints after transverse impact.

In overall, it is found that most of the existing studies mainly focused on thermoset composite joints under in-plane static and dynamic loads. However, up to date, few attempts have been made to investigate the impact behaviour of thermoplastic composite based mechanical joints in the out-of-plane loading conditions. In practice, there will be the cases, in which the single-lap joint is subjected to out-of-plane loading, typically in an overlap region. When this is the case, the bending moment and shear force will result in severe peeling stress concentration at the debonding tip, with possible delamination being triggered on composite laminates.

Based on No. 216 in the Federal Motor Vehicle Safety Standard [22], there are two typical out-of-plane loading conditions, i.e. the quasi-static concentrated loading and impact loading on vehicle body structures. Thus, this paper aims to firstly investigate the out-of-plane impact and concentrated loading response of the single-lap double rivet joints (SLDJ) with and without adhesive, which are made by woven fibre reinforced thermoplastic composites. Based on the previous research work [16-18, 20, 21, 23, 24], three impact energies of 8, 10 and 12 J are chosen to investigate the transverse impact response of the composite joints. Then, the finite element models are developed to predict the impact response of the

joints. The stress-strain constitutive relationships, damage initiation and evolution, as well as strain-rate effects on the impact response of the joint are implemented in the commercial code Abaqus/Explicit using a VUMAT subroutine. Although the polymer matrix of composite material shows some viscoelastic behaviour, the viscoelastic response of composite materials under low velocity impact can be ignored [25] The simulated out-of-plane impact response of the thermoplastic composite joints are compared with the experimental results in reasonably good correlation. The validated numerical models are further employed to investigate the effects of the boundary condition, impact energies and ply angle on the impact resistance of the composite joints.

2. Experimental work and results

2.1. Materials and specimen preparation

The thermoplastic composite laminated sheet used in the experiments is woven E roving glass fibre reinforced polypropylene (GFPP) provided by Bond Laminates Ltd (Germany). The specimens are processed using a waterjet cutting machine (MAXIEM 1530). The parameters used include the hydraulic pressure of 207 MPa, the average feed rate of 636 mm/min, and the abrasive mass flow rate of 420 g/min. The end tabs for clamping and supporting purposes are made from the same material. The bonding area of the specimen was polished using p80, p200, p400 sandpaper in sequence and then cleaned using acetone. The tabs and laminates were bonded using the structural epoxy XA120 adhesive film, with a curing temperature of 80 °C for 16 hours and a post-cure temperature of 120 °C for 1 hour. The fasteners used in this study were Hi-Lok threaded Pin (EN6115-3), in combination with a threaded self-locking collar (ASNA2528) made of titanium alloy TiAl6V4 (supplied by Airbus). The threaded end of the pin is recessed with a hexagon socket to allow installation from one side. The collar is designed such that its hex

head will be sheared off on installation at a predetermined torque level.

As there are no standards related to this kind of experiments, the methodology used in Ref. [20] and the ASTM D5961/D5961M-17 [26] were referenced in the specimen configuration design, as shown in Fig. 2. Three samples were tested for each condition and all experiments were conducted at room temperature, which is summarized in Table 1.

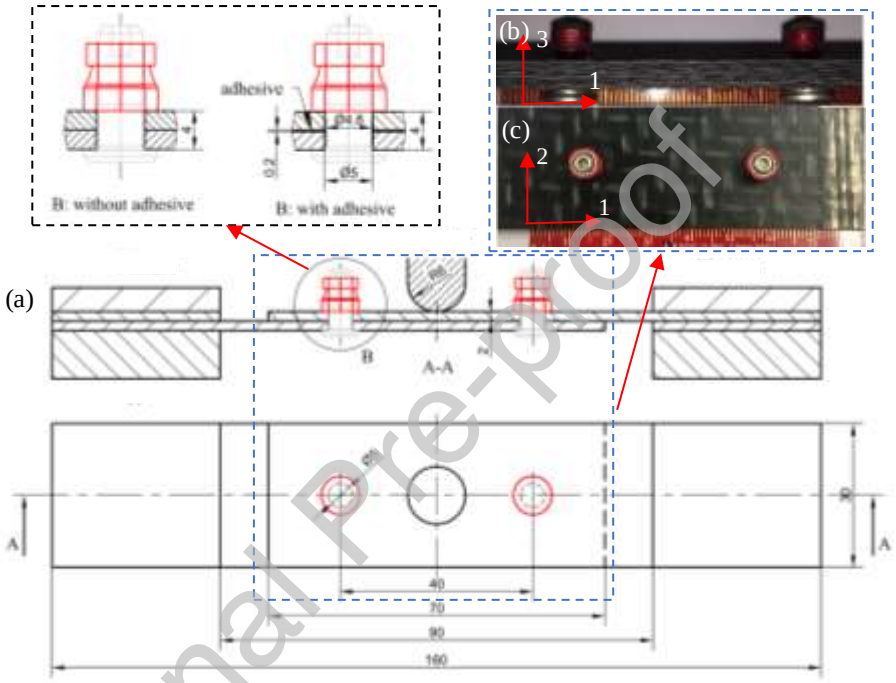

Fig. 2. Specimen configurations (all dimensions in mm): (a) Detailed dimension; (b) Side view; (c) Top view of the experimental joint structure.

Table 1. Summary of the test conditions for impact and quasi-static concentrated loading tests.

	Impact energy	Loading velocity	Sample number
Joints without adhesive	8 J	2.27 m/s	3
	10 J	2.53 m/s	3
	12 J	2.77 m/s	3
Joints with adhesive	8 J	2.27 m/s	3
	10 J	2.53 m/s	3
	12 J	2.77 m/s	3
Joints without adhesive	-	2 mm/min	3
Joints with adhesive	-	2 mm/min	3

2.2. Quasi-static mechanical tests and results

Concentrated loading tests of the composite joint were carried out using a universal test machine of Instron 5985 with a capacity of 150 kN, as shown in Fig. 3(a), to obtain the structural response of the joint

under quasi-static out-of-plane bending load. The full-field image analysis method, i.e. Digital Image Correlation (DIC), was used to capture the displacement field through the thickness direction at the joint area. The surface of each specimen is first coated with a thin layer of white paint. A fine, high contrast speckle pattern of black paint was then sprayed on the white surface. A typical random speckle pattern applied through the thickness direction of the composite joint is shown in the red rectangular region in Fig. 3(b). The displacement loading rate was set to 2 mm/min and the test was terminated until there was a significate load drop.

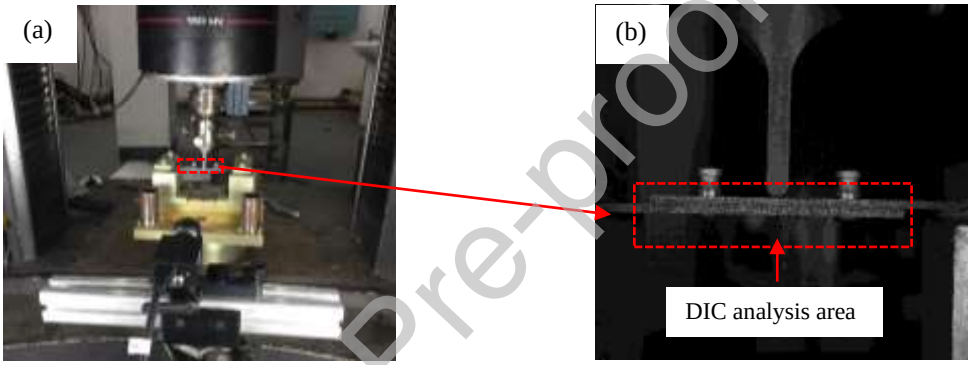

Fig. 3. Photographs of the experiment: (a) Concentrated loading test setup; (b) DIC analysis area.

Quasi-static bending test results are shown in Fig. 4. Each displacement field captured by DIC in Fig. 4(b) and Fig. 4(c) stays at the same key point corresponding to the load-displacement curves. There are three stages of failure in the curves for both the rivet joint (rivet slip, hole failure and laminate break) and the rivet joint with adhesive (debonding, rivet slip and laminate break). The rivet slip was caused by the clearance between the hole on the GFPP sheet and the rivet. It can be seen that the GFPP composite rivet joint with adhesive has a higher stiffness prior to the debonding initiates. The failure of the adhesive between the two laminates caused a significant reduction in load transfer, which resulted in a high tensile load on the bottom laminate. After reaching the peak load, the rivet joint could still transfer some load by the lower laminate, whilst the load on the rivet joint with adhesive dropped sharply.

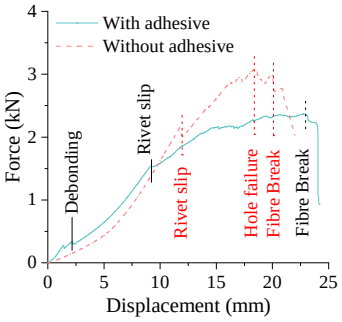

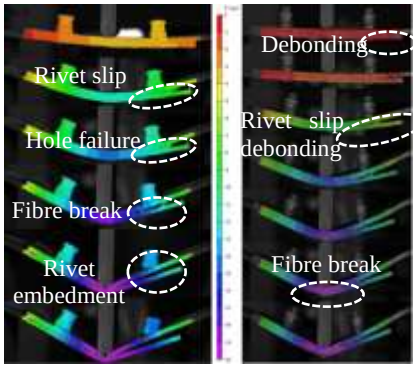

(a) Load-displacement response (b) Rivet joint (c) Rivet with adhesive

Fig. 4. Load-displacement traces of the two types of joints under concentrated loading.

2.3. Projectile impact tests and results

The impact response of the composite joint was investigated using a drop-weight tower, as shown in Fig.5. Two types of specimens were tested, namely the composite rivet joint (SLDJI) and the composite rivet joint with adhesive (SLDJMI). Hemispherical impactor with a diameter of 12 mm was employed to test the specimens. Impact energy levels of 8 Joules (J), 10 J and 12 J were selected to determine the impact response of the thermoplastic composite joint. The impact force was measured using a Kistler 9021A piezo-electric load cell, located just above the impactor. The velocity and displacement of the impactor and the sample deformation were traced by using a high-speed camera, positioned in the front of the drop-weight tower. High-speed footage was recorded at 12,000 frames per second, and the resulting images were analysed by using the software ProAnalyst.

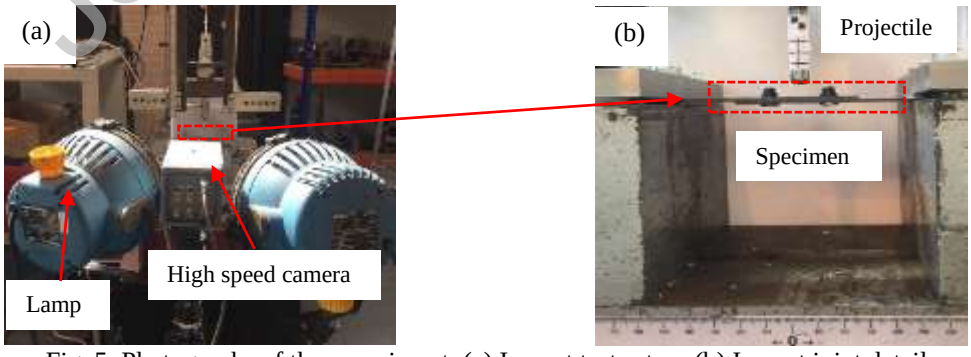

Fig. 5. Photographs of the experiment: (a) Impact test setup; (b) Impact joint detail.

The impact behaviour of the GFPP composite joint was analysed in terms of the peak load, peak

deflection and load-displacement trace. Fig. 6 shows the load-displacement traces of the impact responses of the joint with and without adhesive. It indicates that the rebound of the impactor from the GFPP composite joint after the peak load occurs for all experimental results. The peak loads of 1819, 1934 and 2416 N are recorded in the rivet GFPP composite joint, corresponding to impact energies of 8 , 10 and 12 J, respectively. It shows that there are similar trends on the load-displacement charts for both joint structures. The peak loads corresponding to those impact energies for the rivet joint with adhesive are 1703, 1759 and 2009 N, respectively. As the impact energies below 12 J (i.e. 8 J and 10 J) do not cause the ultimate failure of the joint, the peak load tends to increase with an increase in the impact energies within this range studied. There are some fluctuations in the curves especially at the early stage, with the joint with adhesive being fluctuated more, which are likely due to the ringing effect of the load cell under dynamic loading and debonding bewteen the adhesive layers in the joint.

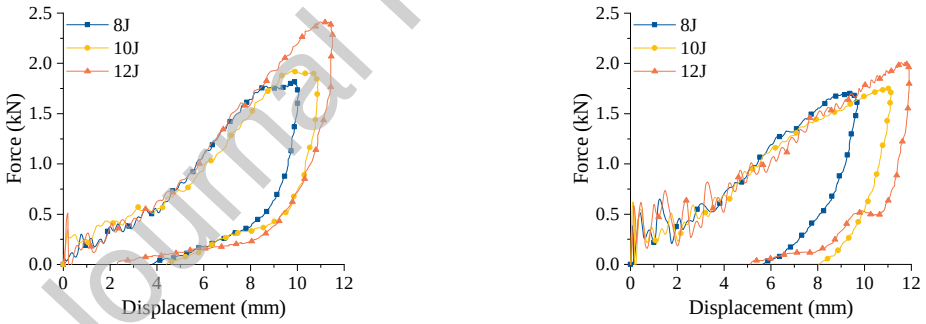

(a) joints without adhesive (b) joints with adhesive

Fig. 6. Load-displacement responses of composite joint with and without adhesive under different impact energies.

The joint with adhesive shows a lower peak load than the joint without adhesive in Fig .6. The total thicknesses of the joints with and without adhesive are the same as 4 mm, as shown in Fig. 2. However, the thickness of the two laminates in the joint with adhesive after polish the surface is reduced to 1.9 mm (the joint thickness is still 4 mm, i.e. 1.9 + 0.2 +1.9). The strength of the GFPP laminate is much higher

than that of the adhesive layer in the thickness direction. Therefore, the reduction of bearing capacity of the GFPP laminate due to the surface treatment cannot be entirely compensated by the thickness of the adhesive layer, although the adhesive will increase the bonding strength between the laminates. The thickness reduction on the laminate is the main reason why the joint with adhesive shows a lower bearing capacity than the joint without adhesive. The high friction force caused by micro-cracks at the interface is proportional to the delamination of the adhesive interface. Thus once the interface is fully delaminated, the surface interaction is governed by a dry friction model [27, 28]. The increased friction force after the debonding in the adhesive layer reduce the load transfer in the joint and limit the stiffness and strength of the joint.

In Fig. 6, the residual displacement for the specimen with adhesive is higher than that without adhesive. For the joint with and without adhesive, there are two ways to prevent the restoration after the impactor rebound, i.e. (1) rivet embedment as shown in Fig.7 (a), (2) the friction force between the laminate surfaces. For the adhesive layer subjected to bending moment and shear force (mode I), the initial microcracks could favourite the crack propagation inside the adhesive layer. As shown in Fig. 7 (b), the dotted lines mean cracks in the adhesive layer and the other areas of the adhesive represent the debonding. The additional debonding produces microcracks in the adhesive layer between the laminates and the cracks in the adhesive layer result in the high friction force between the laminate surfaces. As a result, the recovery of the joint with adhesive after impact is restrained by those bonding. Consequently, the residual displacement for the specimen with adhesive is higher than that without adhesive.

(a) Rivet embedment morphology (dimensions in mm)

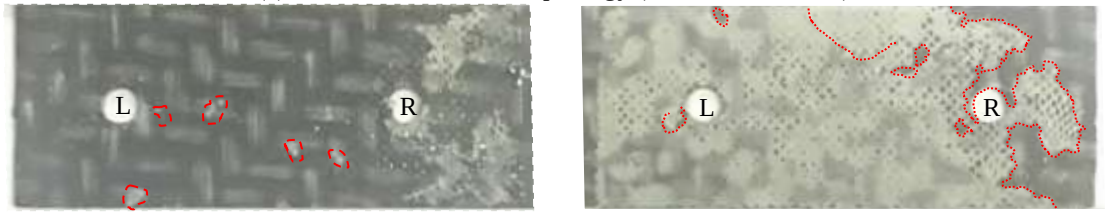

(b) Adhesive debonding and crack morphology

Fig. 7. Typical macro damage morphology of the joint with adhesive under 10 J impact energy.

3. Numerical modelling of the composite joint

The mechanical response of individual constituent materials, i.e. the composite, adhesive layer and titanium alloy, is prescribed via a relevant material model. The composite material model available in the commercial code Abaqus [28] is not suitable for the analysis of the problem investigated here, as it was developed for modelling the in-plane failure of laminated composites, without considering the strain-rate effect. Therefore, to simulate the out-of-plane failure in the composite laminates, a 3D material model, with strain-rate effect, failure initiation and damage evolution, is developed and implemented into the main programme via a user-defined VUMAT subroutine. The titanium alloy rivet is modelled by using Johnson-Cook plasticity, which is available in the commercial code Abaqus [29]. The constitutive response of the adhesive layer is defined by using a traction-separation description available in Abaqus through cohesive surface. The assumptions considered to develop the model are as follows:

(1) The viscoelastic, plastic and temperature effects on GFPP composite and adhesive are ignored.

(2) The temperature effect on titanium alloy is ignored.

(3) The bonding between the GFPP composite and epoxy adhesive is modelled without imperfection.

3.1 Modelling of thermoplastic woven composites

3.1.1 Elastic behaviour

The GFPP composite used in the experiment is fabricated from plain weave fabric prepregs, having the same mechanical response in the warp and weft direction. Thus, the macroscopic constitutive behaviour of the woven GFPP composite material is assumed herein as being orthotropic elasticity. The footnotes 1, 2 and 3 denote the in-plane warp, in-plane weft and out-of-plane directions of the plain-woven GFPP material. Therefore, the elastic constitutive relationship can be expressed as:

$$[\boldsymbol{\sigma}]=[\mathbf{C}][\boldsymbol{\varepsilon}]\begin{pmatrix}\sigma_{11}\\ \sigma_{22}\\ \sigma_{33}\\ \tau_{12}\\ \tau_{23}\\ \tau_{13}\end{pmatrix}=\begin{pmatrix}C_{11} & C_{12} & C_{13} & 0 & 0 & 0\\ C_{12} & C_{22} & C_{23} & 0 & 0 & 0\\ C_{13} & C_{23} & C_{33} & 0 & 0 & 0\\ 0 & 0 & 0 & 2G_{12} & 0 & 0\\ 0 & 0 & 0 & 0 & 2G_{23} & 0\\ 0 & 0 & 0 & 0 & 0 & 2G_{31}\end{pmatrix}\begin{pmatrix}\varepsilon_{11}\\ \varepsilon_{22}\\ \varepsilon_{33}\\ \varepsilon_{12}\\ \varepsilon_{23}\\ \varepsilon_{13}\end{pmatrix} \tag{1}$$

where

$$\begin{aligned}
&C_{11}=E_1(1-\nu_{23}\nu_{32})\Gamma\\
&C_{22}=E_2(1-\nu_{13}\nu_{31})\Gamma\\
&C_{33}=E_3(1-\nu_{12}\nu_{21})\Gamma\\
&C_{12}=E_1(\nu_{21}+\nu_{31}\nu_{23})\Gamma\\
&C_{23}=E_2(\nu_{32}+\nu_{12}\nu_{31})\Gamma\\
&C_{13}=E_1(\nu_{31}+\nu_{21}\nu_{32})\Gamma\\
&\Gamma=1/(1-\nu_{12}\nu_{21}-\nu_{23}\nu_{32}-\nu_{31}\nu_{13}-2\nu_{21}\nu_{32}\nu_{13})
\end{aligned}
\quad \text{and} \quad
\begin{aligned}
&E_1^d=(1-d_{1t})(1-d_{1c})E_1\\
&E_2^d=(1-d_{2t})(1-d_{2c})E_2\\
&E_3^d=(1-d_{3c})E_3\\
&G_{12}^d=(1-d_{12})G_{12}\\
&G_{23}^d=(1-d_{2t})(1-d_{2c})G_{23}\\
&G_{31}^d=(1-d_{1t})(1-d_{1c})G_{31}
\end{aligned} \tag{2}$$

Here, E_i, G_{ij} and ν_{ij} $(i,j=1,2,3)$ are Young's and shear moduli and Poisson's ratios of the woven GFPP. The material constants of the undamaged GFPP composite material are given in Table 2. In the table, in-plane and out-of-plane moduli, the Poisson's ratios and shear moduli are named as $\boldsymbol{E_1}, \boldsymbol{E_2}, \boldsymbol{E_3}$, $\nu_{12},\nu_{23},\nu_{13}, G_{12},G_{23},G_{13}$ respectively. A 47% glass volume fraction is adopted for the analysis to calculate ν_{23},ν_{13}. E_i^d, G_{ij}^d are the degraded material parameters in Eq. (2).

Table 2. Properties of the GFRR Composite Laminate.

ρ(kg/ m^3)	$E_1=E_2$(GPa)	E_3(GPa)	ν_{12}	ν_{23},ν_{13}	G_{12}(GPa)	$G_{23}=G_{13}$(GPa)
1800	19.63[a]	4.42[b]	0.21[a]	0.34[c]	1.41[a]	1.33[c]

[a] measured by using ASTM D3039/D3039M [30] at loading speed of 1 mm/min
[b] based on compression test at loading speed of 0.125 mm/min
[c] based on Ref. [31] calculated

3.1.2. Continuum failure initiation criteria

The failure of woven composites subjected to low-velocity impact can be characterised by using the well-established criteria used in Refs. [32, 33]. Six different failure conditions are considered to account for various damage modes. These criteria, using a set of quadratic failure functions between the corresponding axial stress and the shear stresses, are employed to determine damage initiation related to all potential failure modes as follows:

$$f_{1t} = \left(\frac{\sigma_{11}}{S^r_{1t}}\right)^2 + \varsigma\left(\frac{\sigma_{12}}{S^r_{12}}\right)^2 + \left(\frac{\sigma_{13}}{S^r_{13}}\right)^2 \geq 1, \quad \sigma_{11} \geq 0 \tag{3}$$

$$f_{2t} = \left(\frac{\sigma_{22}}{S^r_{2t}}\right)^2 + \varsigma\left(\frac{\sigma_{12}}{S^r_{12}}\right)^2 + \left(\frac{\sigma_{23}}{S^r_{23}}\right)^2 \geq 1, \quad \sigma_{22} \geq 0 \tag{4}$$

$$f_{1c} = \left(\frac{\sigma_{11}}{S^r_{1c}}\right)^2 \geq 1, \quad \sigma_{11} < 0 \tag{5}$$

$$f_{2c} = \left(\frac{\sigma_{22}}{S^r_{1c}}\right)^2 \geq 1, \quad \sigma_{22} < 0 \tag{6}$$

$$f_{3c} = \left(\frac{p}{S^r_{3c}}\right)^2 \geq 1, \quad p = \frac{\sigma_{11} + \sigma_{22} + \sigma_{33}}{3} < 0 \tag{7}$$

$$f_{12} = \left(\frac{\sigma_{12}}{S^r_{12}}\right)^2 \geq 1 \tag{8}$$

The footnotes (1, 2, 3, 12 and *t*, *c*) in Eqs. (3)-(8) represent warp, weft, thickness direction, shear plane and tension, compression, respectively. $\sigma_{ij}(i, j = 1, 2, 3)$ and $S^r_{ij}(i = 1, 2, 3, j = t, c, 2, 3)$ are the stresses and the strain-rate dependent strength properties of the woven GFPP, which are provided in Table 3. Based on the studies from Refs. [25, 34-36], GFPP is strain-rate sensitive. The strain-rate effect is accounted in accordance with the following relationship:

$$S_{ij}^{r}(\dot{\varepsilon}) = S\left(1 + R_{ij}\,\mathrm{In}\frac{|\dot{\varepsilon}_{ii}|}{\dot{\varepsilon}_0}\right) \tag{9}$$

where S_{ij} and R_{ij} are the static strengths and strain-rate parameters, respectively. Their values are given in Table 3. The reference strain-rate value of $\dot{\varepsilon}_0 = 1.04\times10^{-4}\ s^{-1}$, which is based on the experiment, is used in the modelling. Mechanical properties of the composite laminates are determined according to the Ref. [30] by a series of experiments, including tensile and shear tests. Three specimens were tested for each type of experiments. The tensile and shear strengths in Table 3 are measured from the tests, and the compressive strengths are based on the same type of GFPP on Ref. [25].

Table 3. Static strength values and strain-rate coefficients of GFPP Laminates.

	$S_{1t} = S_{2t}$	$S_{1c} = S_{2c}$	S_{3c}	S_{12}	$S_{23} = S_{31}$
S(MPa)	405 [a]	315 [b]	440 [a]	113 [a]	150 [b]
R [25]	0.089	0.181	0.005	-0.061	0.005

[a] measured using ASTM D3009/D3039M [30]
[b] based on Ref. [25]

3.1.3 Damage evolution

The method used by Sitnikova et al. [25] is adopted and modified to model the development of the damage variables. It is a simplified model allowing the direct calculation of the total value of the damage variables at each time increment without considering the complicated fracture energy parameters and element characteristic length. At the onset of failure, the damage variables for the corresponding failure mode are calculated as follows:

$$\begin{aligned} d_{it} &= \alpha_1\sqrt{f_{it}-1}, \quad \text{if } f_{it}\geq 1, \quad i=1,2 \\ d_{ic} &= \alpha_2\sqrt{f_{ic}-1}, \quad \text{if } f_{ic}\geq 1, \quad i=1,2 \\ d_{3c} &= \alpha_3\sqrt{f_{3c}-1}, \quad \text{if } f_{3c}\geq 1 \\ d_{12} &= \alpha_{12}\sqrt{f_{12}-1}, \quad \text{if } f_{12}\geq 1 \end{aligned} \tag{10}$$

The parameters $\alpha_1,\alpha_2,\alpha_3,\alpha_{12}$ in Eq. (12) govern the rate of growth of the damage variables, which are determined by parametric studies, where the value of one of $\alpha_1,\alpha_2,\alpha_3,\alpha_{12}$ was varied, whilst the

remaining parameters were fixed. The predictions were compared with the experimental force-displacement traces, with this process ongoing until reasonable correlation was obtained to gain those parameters. In this study, $\alpha_1 = 0.3, \alpha_2 = 0.6, \alpha_3 = 0.4, \alpha_{12} = 0.2$.

3.2 Modelling of the adhesive layer

The cohesive surface-based damage [25] is adopted to simulate the debonding failure of the adhesive interface. The constitutive response of the adhesive layer is defined by using a traction-separation description of cohesive elements. Damage initiation is defined by a quadratic nominal stress criterion, as follows:

$$\left(\frac{t_n}{t_n^0}\right)^2 + \left(\frac{t_s}{t_s^0}\right)^2 + \left(\frac{t_t}{t_t^0}\right)^2 = 1 \tag{11}$$

where t_n, t_s and t_t are the current normal and shear stresses, t_n^0, t_s^0 and t_t^0 are the peak nominal stresses in the appropriate directions.

Damage evolution is defined via a power law as follows:

$$G_n^C + \left(G_s^C - G_n^C\right)\left(\frac{G_s^C + G_t^C}{G_s^C + G_n^C}\right)^\eta = 1 \tag{12}$$

where G_n, G_s and G_t denote the work done by the tractions and their conjugate relative displacements in the normal and the two shear directions, and G_n^c, G_s^c and G_t^c are their associated critical fracture energies. The cohesive interface parameter values are given in Table 4. The friction force caused by adhesive micro-cracks is modelled using the coupled cohesive-friction method, which is available in Abaqus/Explicit [28].

Table 4. Cohesive surface properties [25].

ρ(kg/m^3)	E_n(GPa)	$E_s = E_t$(MPa)	t_n^0(MPa)	$t_s^0 = t_t^0$(MPa)	G_n^c(J/m^2)	$G_s^c = G_t^c$(J/m^2)
920	10	4	70	100	300	700

3.3 Modelling of the rivet

The behaviour of the titanium alloy rivet is modelled by using the Johnson-Cook plasticity model [37], along with the linear evolution of the damage variable with effective plastic displacement. As the temperature effect of titanium alloy rivet is neglected in the low-velocity impact experiment and static concentrative loading test, the appropriate expressions can be simplified as:

$$\bar{\sigma} = \left[A + B\left(\bar{\varepsilon}_{pl}\right)^{n}\right]\left[1 + C\ln\left(\frac{\dot{\bar{\varepsilon}}_{pl}}{\dot{\varepsilon}_{0}}\right)\right] \tag{13}$$

$$\bar{\varepsilon}_{D}^{pl} = \left(d_1 + d_2 e^{d_3 p/q}\right)\left[1 + d_4 \ln\left(\frac{\dot{\bar{\varepsilon}}_{pl}}{\dot{\varepsilon}_{0}}\right)\right] \tag{14}$$

where $\bar{\sigma}$ is the yield stress, $\bar{\varepsilon}_{pl}$ is the equivalent plastic strain, $\dot{\bar{\varepsilon}}_{pl}$ is the equivalent plastic strain rate, A, B, n and C are material parameters, $\dot{\varepsilon}_0 = 1.0\ \mathrm{s}^{-1}$ is the reference strain rate, $\bar{\varepsilon}_D^{pl}$ is the equivalent plastic strain at the onset of damage and d_1-d_4 are failure parameters, p/q is a dimensionless pressure-deviatoric stress ratio (where p is the pressure stress and q is the Mises stress). The material parameters of the titanium alloy are provided in Table 5.

Table 5. Johnson-Cook model parameters for the titanium alloy [37].

ρ(kg/m^3)	E(GPa)	ν	A(MPa)	B(MPa)	n	C	d_1	d_2	d_3	d_4
4430	110	0.33	862	331	0.34	0.012	-0.09	0.25	-0.5	0.014

3.4 Validation of the numerical models

In general, the FE simulation of impact response of composites with damage is often mesh sensitive when the fracture energy and characteristic length parameters were ignored. Therefore, to address this the mesh sizesensitivity analysis was conducted. Here, three different mesh sizes on the impact response were studied, which include fine mesh size (0.27 mm × 0.41 mm × 0.16mm, F-Mesh), medium mesh size (0.35mm × 0.68 mm × 0.25 mm, M-Mesh) and coarse mesh size (0.53 mm × 0.68 mm × 0.5 mm,

C-Mesh). The simulation results are compared with the experimental results in Fig. 8. The observation of the figure shows that with the mesh size studied, the impact response, in terms of force – displacement trace, is quite similar. Although the simulation results related to the fine mesh correlated slightly better to the experimental results than the medium mesh counterpart, by considering both computational efficiency and accuracy, the medium mesh size (0.35mm × 0.68 mm × 0.25 mm) was selected.

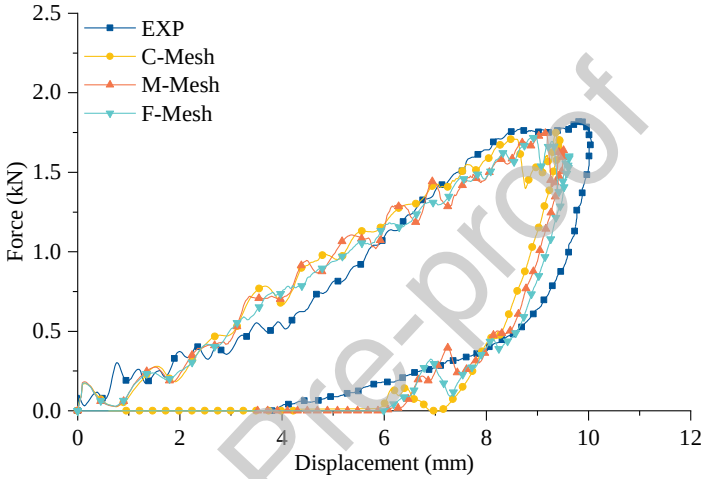

Fig. 8. Mesh convergence analysis at 8 J impact energy

Each of these models, as shown in Fig. 9, consists of a rigid impactor (with an inertia mass of 3.121 kg specified at a reference point), the GFPP joint structure and two supports. To save the computational cost, the rivet joint is simplified, as shown in Fig. 9(a) and Fig. 9(b). Here, each layer (0.5 mm thick) of the laminates is modelled with two elements through the thickness to capture the response through the thickness direction. The biased fine meshes, as shown in Fig. 9(d), are generated around the impact zone and the hole. All constituent materials are modelled using 8-noded solid elements with reduced integration (C3D8R). A general contact interaction is defined on both the exterior and interior faces of the joint to address possible contact scenarios after an element fails. The coefficients of friction between the composite laminate and impactor, composite plates and rivet joint, support and laminate are set to 0.324,

0.160 and 0.300 [38], respectively. As for the load condition, a predefined initial velocity is applied on the rigid impactor, which is equal to 2.27 m/s for 8 J, 2.53 m/s for 10 J and 2.77 m/s for 12 J impact energy.

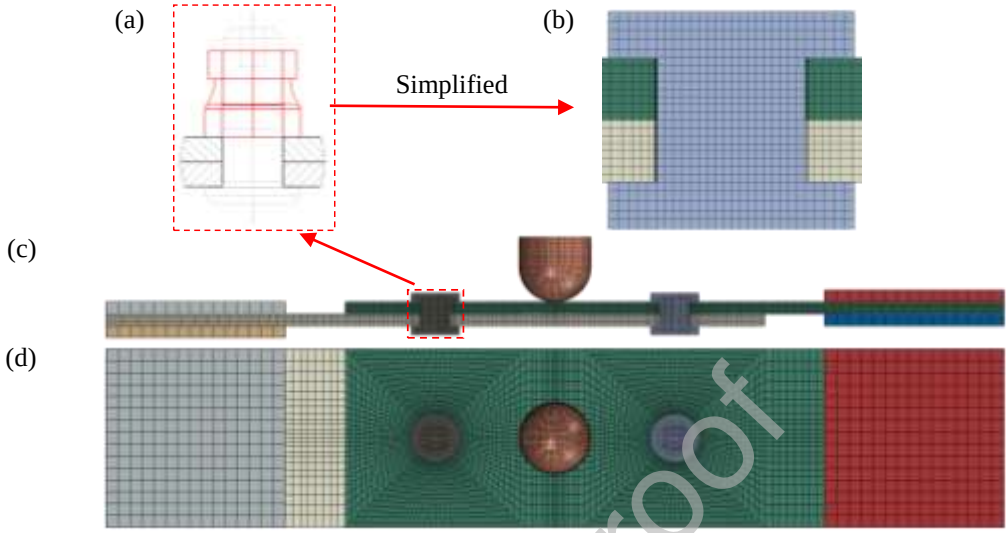

Fig. 9. The whole SLDJI FE model of the composite joint. (a) Schematic of joint, (b) Detailed mesh of simplified rivet and tolerance fit, (c) Side view and (d) Top view of joint.

The laminate in the joint with adhesive is 0.2 mm thinner due to surface polishing. Reduction of the thickness may introduce unexpected change, especially for out-of-plane local loading. Therefore, parametric studies were performed to investigate the influence of the laminate thickness on the impact response of the joint with adhesive. Here, joints with three different laminate thicknesses subject to 8 J impact energy were numerically analysed, with results shown in Fig. 10. It can be seen that with decreasing the laminate thickness, the peak contact load decreases mildly (5.6%) and the maximum displacement increases slightly (4.1%).

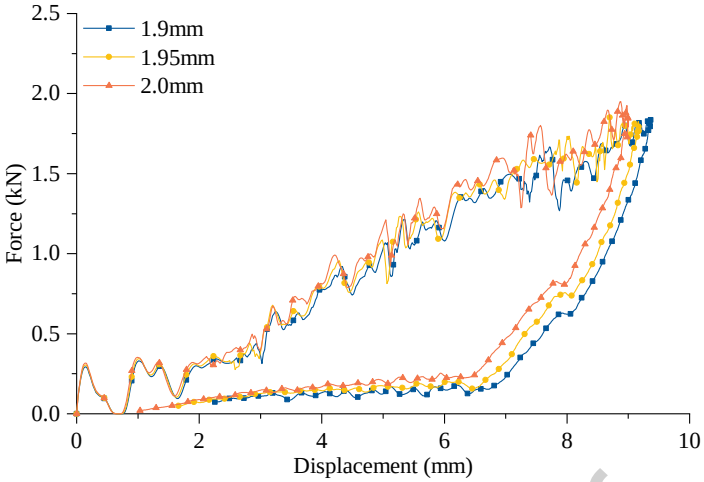

Fig. 10. Influence of laminate thickness on the impact response for joint with adhesive.

The experimental and numerical load-displacement traces are compared in Fig. 11. The numerical responses are in good agreement with the experimental results in terms of peak load, maximum displacement and rising and falling trends under different impact energies. These curves are of an enclosure form attributed to the rebound of the projectile, which provide essential data to calculate the energy dissipation in the system. Based on the enclosure area, the dissipated energies are 6.88, 8.15 and 9.75 J corresponding to 8, 10 and 12 J impact energies for the rivet GFPP composite joint, and 7.18, 9.59 and 10.62 J for the rivet adhesive GFPP composite joint, respectively.

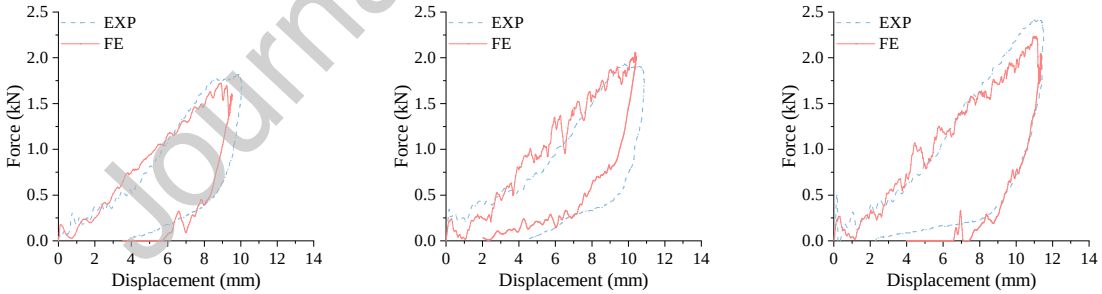

(a) Joints without adhesive under 8 J (left), 10 J (middle), 12 J (right) impact energy, respectively.

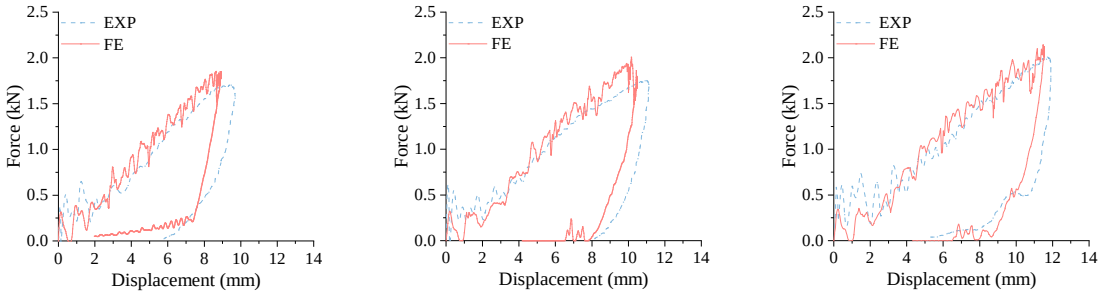

(b) Joints with adhesive under 8 J (left), 10 J (middle), 12 J (right) impact energy, respectively.

Fig. 11. The experimental and numerical load-displacement response of

the joint with and without adhesive.

The simulated displacement profile for the composite rivet joint at the peak load point and its experimental counterpart are compared in Fig. 12. The predicted impactor displacement is 10.4 mm, whilst the experimental measurement is 10.9 mm. The similar displacement modes are exhibited between the simulated and the experimental observations, in terms of joint peeling and bending. In general, the numerical response predicted matches with the experimental one reasonably well.

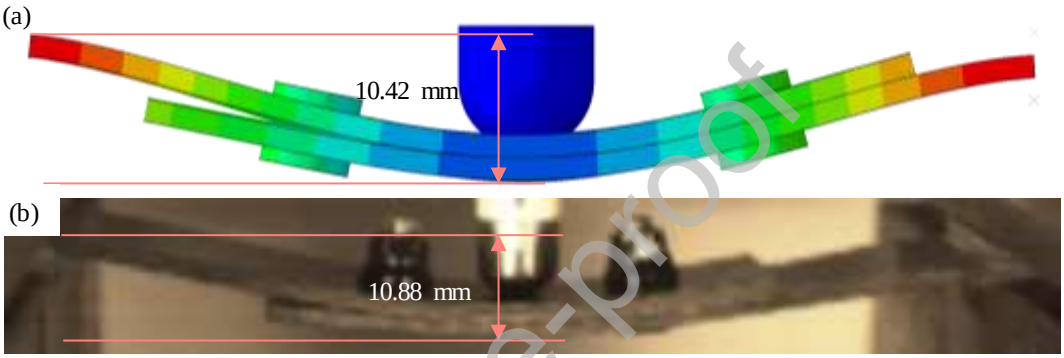

Fig. 12. Comparison of maximum deflection of the rivet joint under 10 J impact energy between (a) the FE simulation and (b) the experimental results.

4. Parametric studies

4.1 Effect of boundary condition on the impact resistance of the joint

As the peak load is underestimated because some slips exist in the grip area of the joint, the maximum displacement and the dissipated energy are therefore overestimated. It is worth investigating the effect of the boundary on the impact response of the joint. Fig. 13 shows the modified FE model, in which the fixture and the support are not simulated, and the two ends of the laminate are fixed to eliminate the relative slip. In the modified FE model, the only modification is the end boundary conditions, while material parameters, mesh size, loading conditions are kept unchanged. Hence, it is reasonable that the modified FE model can be used to help understand the quantitative response of a woven thermoplastic composite joint subjected to an out-of-plane load.

Fig. 13. The modified FE model used to eliminate slip.

As a result, the damage variables and locations are quite different for the modelling outputs in relation to different boundary conditions. Table 6 provides the comparison of joint damage variables and the magnified damaged zone for the joint subjected to 8 J impact energy. The damaged zone can be divided into three areas, namely the area under the impactor and the areas around the laminate holes. Compared with the previous FE model, the damaged areas are concentrated around the peripheral surface of the rivet hole. The bending moment in the previous FE model is higher than that in the modified model due to the slippage between the fixtures and the laminate tapes, so that the embedment deformations around the rivet hole are more severe. These phenomena tend to be eliminated since the embedment caused by bending leads to a decreased contact surface area. This results in the stress concentration between the rivet nut and the laminate. It can be seen in Table 6 that the damage variables in the modified FE distribute more evenly than the counterpart. For both the FE models, there is no compressive failure in the weft direction.

Table 6. Comparison of damage variables between the SLDJI FE and the modified FE models subjected to 8 J impact energy (at the moment of complete separation between the impactor and composite laminate).

The SLDJI FE	The modified SLDJI FE
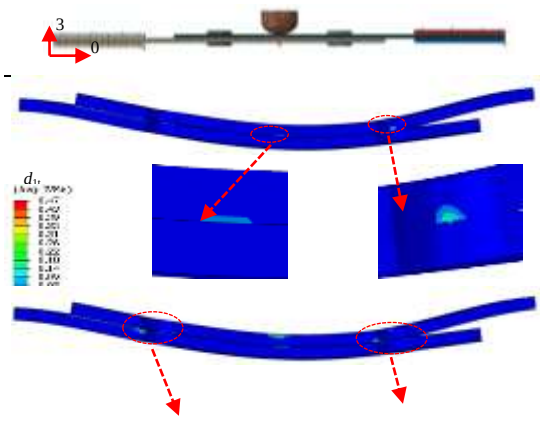	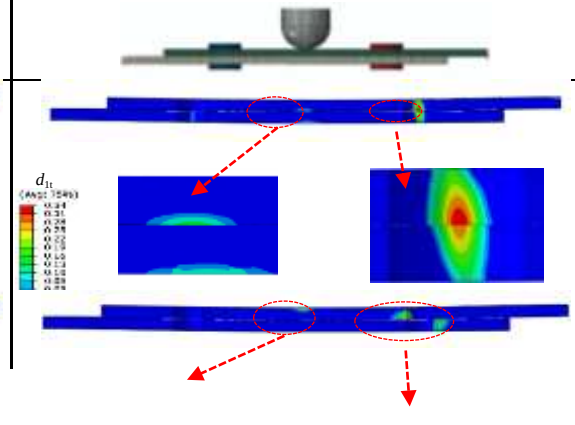

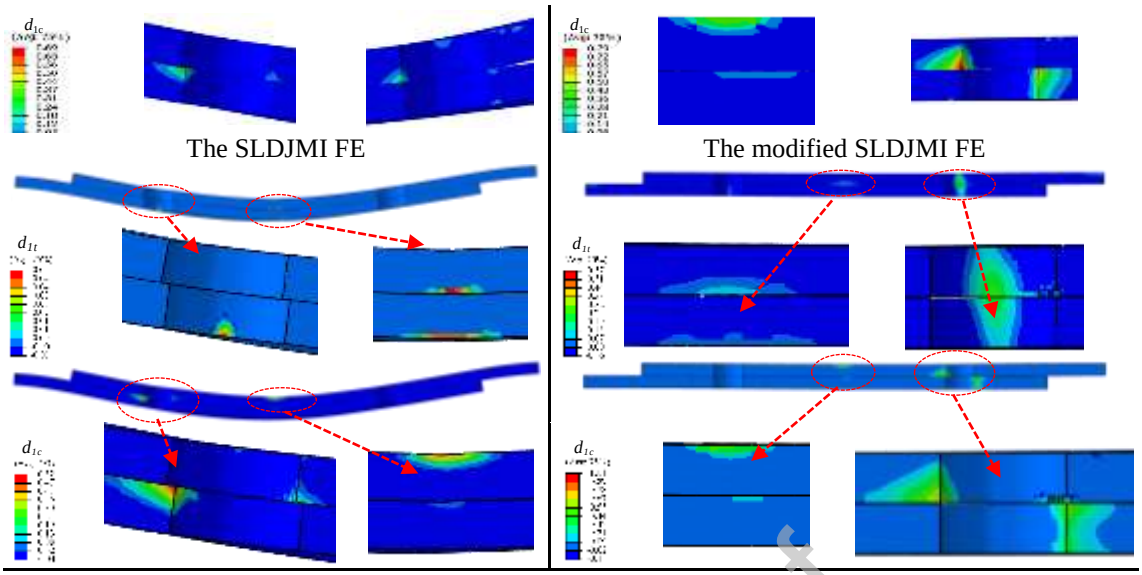

4.2 Effect of ply angle on the impact resistance of the joint

Fig. 14 shows that the load-carrying capacities are almost the same for 45° ply angle and 0° ply angle woven laminate joint structures. The predicted peak loads of 1.66, 1.99 and 2.21 kN are obtained in the case of 45° ply SLDJI FE model corresponding to impact energies of 8, 10 and 12 J, whilst the 0° ply counterparts are 1.72, 2.06 and 2.24 kN. The difference on the peak loads for 0° ply and for 45° ply are small (<4 %), as shown in Fig. 14. The load-displacement responses are in a similar pattern corresponding to the three impact energies, but with increasing the peak force. The joint with adhesive has the same trend.

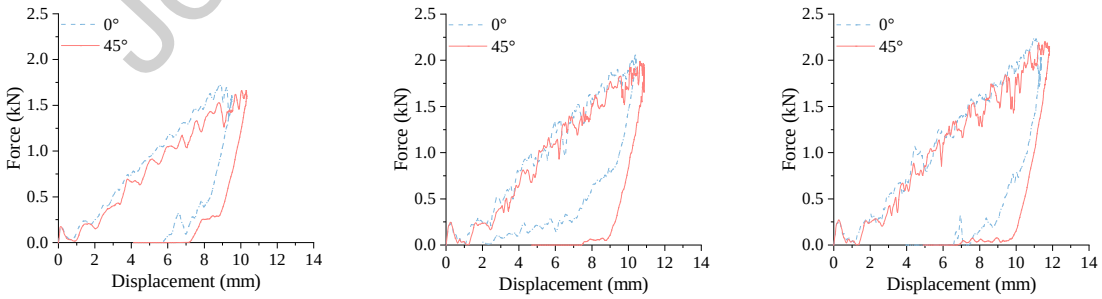

(a) Response of SLDJI under 8 J (left), 10 J (middle), 12 J (right) impact energy.

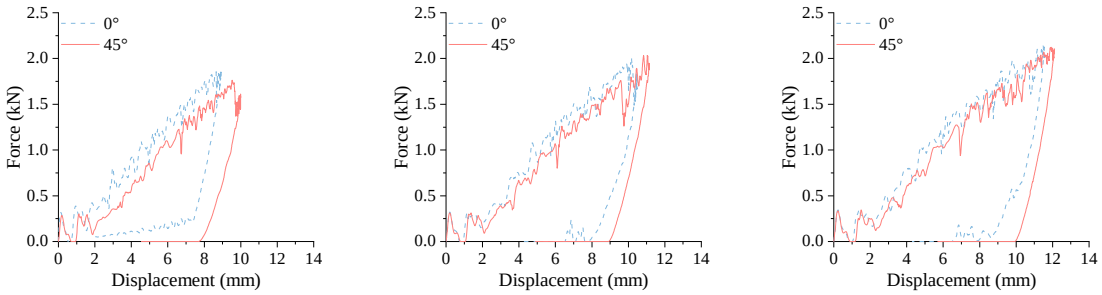

(b) Response of SLDJMI under 8 J (left), 10 J (middle), 12 J (right) impact energy.

Fig. 14. The FE load-displacement response of the FE with 0°and 45°ply angles.

An apparent difference between the response of 0° and 45° ply angle in Fig. 14 is the maximum displacement. There are consistently higher displacement values for the 45° ply. The maximum displacement is governed by the coupled bending, shear and membrane stiffnesses, which are dependent on the Young's moduli of materials [39]. The polar properties of laminate stiffness in Fig. 15 shows the in-plane laminate engineering constant rotated by 0 to 360 degree [40]. Fig. 15 highlights the anisotropy of the laminate and the influence of the orientation. The laminate stiffness in the 0° direction for the 0° ply is larger than the 45° ply counterpart, as shown in Fig. 15 (a) and Fig. 15 (b). As the result, the maximum displacement for 45° ply is higher in comparison to 0° ply.

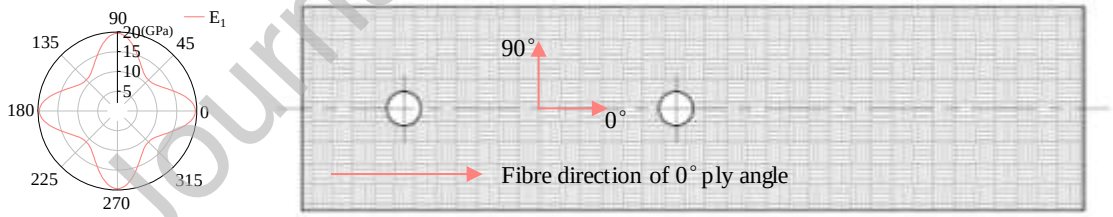

(a) 0° ply angle laminate structure

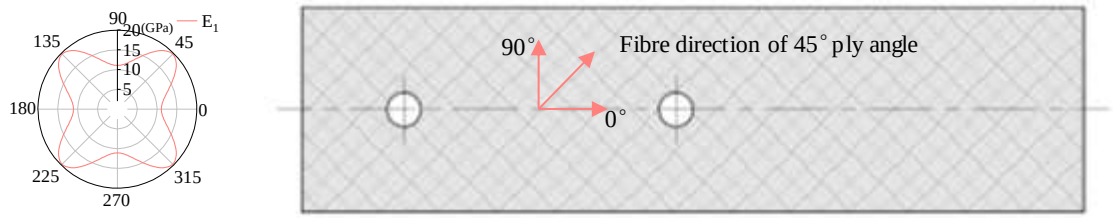

(b) 45° ply angle laminate structure

Fig. 15. Polar properties of structure stiffness distribution.

4.3 Effect of impact energy on the impact resistance of the joint

Fig. 16 shows the trend of the peak load, maximum deflection, and dissipated energy responses

versus impact energy. The impact response of the joint can be divided into two stages with the impact energy up to 16 J, i.e. the initial damage at the impact energy of 12 J (reflected by the lower slope of impact energy – peak load curve) and the ultimate damage at the threshold energy of 16 J (shown as a flat feature of impact energy – peak load curve from 16 J to 20 J). Prior to the threshold impact energy, the change of dissipated energy is at a low pace, and the increase of the peak load and the maximum deflection are at a high rate. The energy is dissipated in two manners during the impact for the joint without adhesive, i.e. friction in the contact surface and damage of the composite material.

It can be seen from Fig. 16 that at the initial damage (12 J impact energy) there are some local bearing failures of the laminate at the contact regions between the right rivet and laminates. With the increase of the impact energy from 12 J to 16 J, i.e. the ultimate threshold energy, the rivet at the right hand side begins to penetrate into the composite laminates. One extra point corresponding to 20 J impact energy is added to show that the peak load at this impact energy is similar to that at 16 J, indicating the ultimate failure occurring at this impact energy. However, the rivet at the right hand side has penetrated into the composite laminates, accompanied with separation of laminates and more severe embedment damage, the deflection and dissipated energy still increase due to the extended damage of the materials and rotation of rivets.

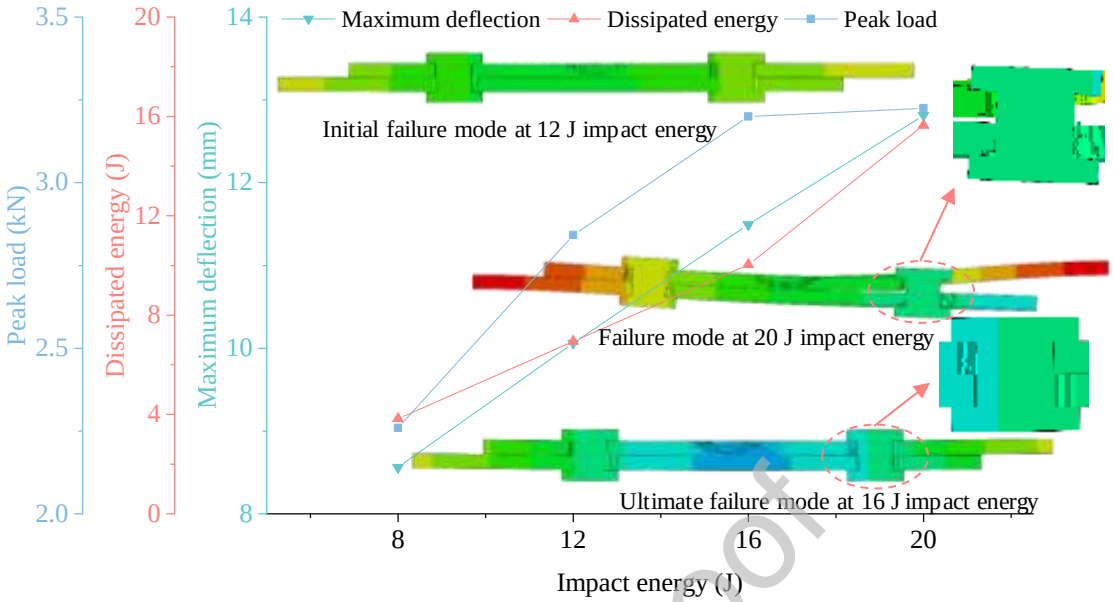

Fig. 16. Comparison of the response of the joint without adhesive under different impact energy.

5. Conclusions

In this paper, experimental investigation and numerical analysis have been presented on the thermoplastic single-lap rivet joints with and without adhesive subjected to out-of-plane loading. Firstly, three-point quasi-static bending tests with DIC analyses and projectile impact tests with different impact energies on the joints have been conducted. The experimental results of the rivet joints without adhesive under the bending show that there are three stages of failure in the load-displacement trace, i.e. the rivet slip, hole failure and laminate break, whilst the failure of the joint with adhesive is characterised with the debonding/rivet slip, hole failure and laminate break. The rivet joint with adhesive has a higher stiffness prior to debonding initiation; however, its out-of-plane load-carrying capacity is slightly lower than the rivet only counterpart. The peak load of the rivet joint with adhesive is 7 - 20 % lower than that of the joint without adhesive at the same impact energy level. The cliff-like reduction of the load after failure initiation on the adhesive joint also needs to be taken into consideration for practical applications. In the

impact response of the joint, the initial microcracks and debonding in the adhesive layer attribute to more energy dissipation. The increased friction force after the debonding and cracks in the adhesive layer reduce the load transfer in the joint and give a slightly lower strength of the joint in comparison to the joint without adhesive.

Finite element models developed have been validated against the corresponding experimental results with reasonably good correlation. The numerical modelling results using the validated models indicate that boundary slip causes the laminate to withstand a large bending moment and reduces the contact area between rivet nut and laminate hole, which contributes to the stress concentration and local failure around the laminate hole. The differences of the peak loads between 0° ply and for 45° ply are small (<4 %), whereas the energy dissipation for 45° ply on the laminate is higher up to 11 % than the 0° ply counterpart. It is shown that below the threshold impact energy, energy dissipates at a low pace and the peak load and maximum deflection increase at a high rate, which means that the thermoplastic composite joint has a good impact resistance at this condition.

Acknowledgements

The authors would like to thank the financial support provided by the National Natural Science Foundation of China (Grant number 11672105) and National Innovation Research Group of China (Grant number 51621004). The first author, Chao Chen, gratefully acknowledges the financial support from the China Scholarship Council (CSC) under Grant number 201706130108.

Declaration of Interest statement

The authors declared no conflict of interest with respect to the research, authorship and publication of this article.

References

[1] T. Ishikawa, K. Amaoka, Y. Masubuchi, T. Yamamoto, A. Yamanaka, M. Arai, J. Takahashi, Overview of automotive structural composites technology developments in Japan, Composites Science and Technology, 155 (2018) 221-246.

[2] H. Li, Y. Niu, Z. Li, Z. Xu, Q. Han, Modeling of amplitude-dependent damping characteristics of fiber reinforced composite thin plate, Applied Mathematical Modelling, 80 (2020) 394-407.

[3] T. Grätzl, Y. van Dijk, N. Schramm, L. Kroll, Influence of the automotive paint shop on mechanical properties of continuous fibre-reinforced thermoplastics, Composite Structures, 208 (2019) 557-565.

[4] A. Elmarakbi, Advanced Composite Materials for Automotive Applications : Structural Integrity and Crashworthiness, Wiley, Hoboken, 2013.

[5] https://www.compositesworld.com/articles/is-the-bmw-7-series-the-future-of-autocomposites.

[6] M.A. McCarthy, C.T. McCarthy, V.P. Lawlor, W.F. Stanley, Three-dimensional finite element analysis of single-bolt, single-lap composite bolted joints: part I—model development and validation, Composite Structures, 71 (2005) 140-158.

[7] G. Ger, K. Kawata, M. Itabashi, Dynamic tensile strength of composite laminate joints fastened mechanically, Theoretical and applied fracture mechanics, 24 (1996) 147-155.

[8] Q. Li, R. Mines, R. Birch, Static and dynamic behaviour of composite riveted joints in tension, International journal of mechanical sciences, 43 (2001) 1591-1610.

[9] G.M. Pearce, A.F. Johnson, R.S. Thomson, D.W. Kelly, Numerical Investigation of Dynamically Loaded Bolted Joints in Carbon Fibre Composite Structures, Applied Composite Materials, 17 (2009) 329-346.

[10] B. Egan, C.T. McCarthy, M.A. McCarthy, P.J. Gray, R.M. O'Higgins, Static and high-rate loading of single and multi-bolt carbon–epoxy aircraft fuselage joints, Composites Part A: Applied Science and Manufacturing, 53 (2013) 97-108.

[11] S. Heimbs, S. Schmeer, J. Blaurock, S. Steeger, Static and dynamic failure behaviour of bolted joints in carbon fibre composites, Composites Part A: Applied Science and Manufacturing, 47 (2013) 91-101.

[12] N. Perogamvros, G. Lampeas, Experimental investigation of composite lockbolt fastened joints under in-plane low velocity impact, Composites Part A: Applied Science and Manufacturing, 90 (2016) 510-521.

[13] A.M. Croxford, P. Davidson, A.M. Waas, Influence of hole eccentricity on failure progression in a double shear bolted joint (DSBJ), Composites Science and Technology, 168 (2018) 179-187.

[14] D. Song, Y. Li, K. Zhang, P. Liu, H. Cheng, T. Wu, Stress distribution modeling for interference-fit area of each individual layer around composite laminates joint, Composites Part B: Engineering, 78 (2015) 469-479.

[15] C. Chen, D. Hu, Q. Liu, X. Han, Evaluation on the interval values of tolerance fit for the composite bolted joint, Composite Structures, 206 (2018) 628-636.

[16] H. Kim, T. Kayir, S.L. Mousseau, Mechanisms of Damage Formation in Transversely Impacted Glass-Epoxy Bonded Lap Joints, Journal of Composite Materials, 39 (2005) 2039-2052.

[17] O. Sayman, V. Arikan, A. Dogan, I.F. Soykok, T. Dogan, Failure analysis of adhesively bonded composite joints under transverse impact and different temperatures, Composites Part B: Engineering, 54 (2013) 409-414.

[18] R.S. Choudhry, S.F. Hassan, S. Li, R. Day, Damage in single lap joints of woven fabric reinforced polymeric composites subjected to transverse impact loading, International journal of impact engineering, 80 (2015) 76-93.

[19]H. Park, H. Kim, Damage resistance of single lap adhesive composite joints by transverse ice impact, International Journal of Impact Engineering, 37 (2010) 177-184.

[20] W. Wu, Q. Liu, Z. Zong, G. Sun, Q. Li, Experimental investigation into transverse crashworthiness of CFRP adhesively bonded joints in vehicle structure, Composite Structures, 106 (2013) 581-589.

[21] X. Liu, X. Shao, Q. Li, G. Sun, Experimental study on residual properties of carbon fibre reinforced plastic (CFRP) and aluminum single-lap adhesive joints at different strain rates after transverse pre-impact, Composites Part A: Applied Science and Manufacturing, 124 (2019) 105372.

[22] U.S. Department of Transportation National Highway Traffic Safety Administration FMVSS No. 216; Roof Crush Resistance.

[23] B. Liao, L. Jia, J. Zhou, H. Lei, R. Gao, Y. Lin, D. Fang, An explicit-implicit combined model for predicting residual strength of composite cylinders subjected to low velocity impact, Composite Structures, 247 (2020) 112450.

[24] B. Liao, J. Zhou, Y. Li, P. Wang, L. Xi, R. Gao, K. Bo, D. Fang, Damage accumulation mechanism of composite laminates subjected to repeated low velocity impacts, International Journal of Mechanical Sciences, 182 (2020) 105783.

[25] E. Sitnikova, Z.W. Guan, W.J. Cantwell, The analysis of the ultimate blast failure modes in fibre metal laminates, Composites Science and Technology, 135 (2016) 1-12.

[26] D5961/D5961M-17, Standard Test Method for Bearing Response of Polymer Matrix Composite Laminates, ASTM International, West Conshohocken, PA, 2017.

[27] D. Garijo, F. Martínez, C.S. Lopes, J. Llorca, C. González, J.L. Puente, J.A. Loya, J. Toral-Vázquez, V. Votsios, E. Martino, Multiscale FE Modelling and Design of Composite Laminates Under Impact, in: P.W.R. Beaumont, C.H. Zweben (Eds.) Comprehensive Composite Materials II, Elsevier, Oxford, 2018, pp. 219-238.

[28] I. Guiamatsia, G.D. Nguyen, A thermodynamics-based cohesive model for interface debonding and friction, International Journal of Solids Structures, 51 (2014) 647-659.

[29] D. Systèmes, Abaqus Analysis User's Guide, Version 6.14, Dassault Systèmes, 2014.

[30] D3039/D3039M-17, Standard Test Method for Tensile Properties of Polymer Matrix Composite Materials, ASTM International, West Conshohocken, PA, 2017.

[31] K. Rouf, X. Liu, W. Yu, Multiscale structural analysis of textile composites using mechanics of structure genome, International Journal of Solids and Structures, 136 (2018) 89-102.

[32] Z. Xu, F. Yang, Z.W. Guan, W.J. Cantwell, An experimental and numerical study on scaling effects in the low velocity impact response of CFRP laminates, Composite Structures, 154 (2016) 69-78.

[33] J. Zhou, Z. Guan, W.J. Cantwell, The energy-absorbing behaviour of composite tube-reinforced foams, Composites Part B: Engineering, 139 (2018) 227-237.

[34] D. H. Kim, S. Y. Kang, H. J. Kim, H. S. Kim, Strain rate dependent mechanical behavior of glass fiber reinforced polypropylene composites and its effect on the performance of automotive bumper beam structure, Composites Part B: Engineering, 166 (2019) 483-496.

[35] A. Martin, R. Othman, P. Rozycki, Testing and simulation of a polypropylene-glass fibre reinforced woven composite on a wide range of strain-rates, in: EPJ Web of Conferences, EDP Sciences, 2012, pp. 01038.

[36] D. Karagiozova, G.S. Langdon, G.N. Nurick, S. Chung Kim Yuen, Simulation of the response of fibre–metal laminates to localised blast loading, International Journal of Impact Engineering, 37 (2010) 766-782.

[37] Y. Zhang, J.C. Outeiro, T. Mabrouki, On the Selection of Johnson-cook Constitutive Model Parameters for Ti-6Al-4V Using Three Types of Numerical Models of Orthogonal Cutting, Procedia CIRP, 31 (2015) 112-117.

[38] C. Stocchi, P. Robinson, S. Pinho, A detailed finite element investigation of composite bolted joints with countersunk fasteners, Composites Part A: applied science and manufacturing, 52 (2013) 143-150.

[39] W.J. Cantwell, Geometrical effects in the low velocity impact response of GFRP, Composites Science and Technology, 67 (2007) 1900-1908.

[40] ANSYS, ANSYS Composite PrepPost User's Guide Release 18, ANSYS Inc, USA, 2017.